Experimental Demonstration of Staggered Ambiguous SAR Mode for Ship Monitoring With TerraSAR-X

Nertjana Ustalli, *Member, IEEE*, Maxwell Nogueira Peixoto, *Graduate Student Member, IEEE*, Thomas Kraus, Ulrich Steinbrecher, Gerhard Krieger, *Fellow, IEEE*, and Michelangelo Villano, *Senior Member, IEEE*

***Abstract*— Maritime surveillance using synthetic aperture radar (SAR) calls for both wide swath and high resolution. This allows frequent monitoring of large areas with high detection probability and low false alarm rate. Conventional SAR modes are, however, limited in that a wide swath can only be imaged at the expense of a reduced azimuth resolution. Ambiguous SAR modes, based on low pulse repetition frequency (PRF) or continuous variation of short pulse repetition intervals (PRIs) (staggered ambiguous mode), overcome this limitation and allow imaging a wide swath with high resolution for specific ship monitoring applications without the need for digital beamforming (DBF) or multiple receive apertures. This article reports on the demonstration of the staggered ambiguous mode via an experimental acquisition with the TerraSAR-X satellite over the North Sea. Despite technical limitations in the SAR instrument, a ground range swath of 110 km was imaged with an azimuth resolution of 2.2 m, i.e., with a resolution improvement of a factor of 8 with respect to TerraSAR-X ScanSAR mode. Despite the higher disturbance level resulting from the presence of range ambiguities of the sea clutter, a detection probability higher than 0.8 was achieved for small ships of 21 m × 6 m size. Range ambiguities of the ships were furthermore identified based on their position and signature. The detected ships were validated using maritime positioning data from their automatic identification system (AIS). These results motivate the adoption of ambiguous SAR modes in existing and future SAR systems and missions.**

***Index Terms*— Ambiguities, automatic identification system (AIS), high-resolution wide-swath imaging, maritime monitoring, ship detection, synthetic aperture radar (SAR), staggered SAR, TerraSAR-X.**

I. Introduction

SYNTHETIC aperture radar (SAR) images provide a great potential in observing and monitoring the maritime environment [1], [2], [3], [4], [5], [6], [7], [8], [9], [10], [11], [12], [13]. Knowing the position and/or type of a vessel benefits a large user community, which includes authorities involved in maritime traffic control, pollution, fisheries, smuggling, and the defense sector. The most important user requirements are persistence, high detection performance, and responsiveness. The observation frequency can be improved by mapping wider swaths. High detection performance, on the other hand, can be obtained from higher resolution SAR images, as more pixels will be available for a given ship, resulting in more favorable statistics, as discussed in [14]. In addition, onboard processing is a promising solution for ensuring responsiveness by providing very low latencies, which can reduce the time between data acquisition and product delivery to end users.

However, wide-swath coverage and high-resolution imaging pose contradicting requirements on the pulse repetition frequency (PRF). In order to control range ambiguities, the pulse repetition interval (PRI), which is the reciprocal of the PRF, must be greater than the time required to collect returns from the entire illuminated swath. A large PRI, or equivalently a low PRF, on the other hand, limits the unambiguous Doppler bandwidth and therefore the achievable azimuth resolution if azimuth ambiguities have to be controlled [15]. A wide swath can also be mapped with ScanSAR or Terrain Observation by Progressive Scans (TOPS), but the azimuth resolution is still impaired [16], [17], [18], [19]. Digital beamforming (DBF) and multiple aperture recording [20], [21], [22] are promising techniques that overcome these limitations and achieve high-resolution wide-swath images but also imply higher system complexity and costs. Furthermore, the use of co-prime SAR concepts allows for reducing the number of transmitted pulses and the data rate. Azimuth ambiguities of ships are then discriminated by comparing two distinct SAR images generated from the original dataset [23], [24].

In [25], we have proposed two high-resolution wide-swath stripmap SAR modes for ship monitoring that "tolerate" ambiguities, do not require DBF, and can be easily adapted to the existing and planned SAR systems. Both modes, referred to as the low PRF and the staggered (high PRF) ambiguous mode, are able to map a wide swath by using a wide elevation beam on both transmit and receive, which can be obtained through tapering of the antenna aperture [26].

An even larger swath, but with a reduced azimuth resolution, can be obtained with a ScanSAR mode that tolerates azimuth ambiguities, as proposed by NovaSAR [18], [19]. The low PRF ambiguous mode [25] is a stripmap mode with a PRF smaller than the nominal Doppler bandwidth so that it allows

Manuscript received 17 May 2023; revised 29 September 2023; accepted 30 October 2023. Date of publication 16 November 2023; date of current version 29 November 2023. *(Corresponding author: Nertjana Ustalli.)*

The authors are with the Microwaves and Radar Institute, German Aerospace Center (DLR), 82234 Wessling, Germany (e-mail: nertjana.ustalli@dlr.de).

Digital Object Identifier 10.1109/TGRS.2023.3333932

collecting the echo from the wide swath. In this case, the high azimuth resolution is obtained by processing the full Doppler bandwidth corresponding to the antenna size [14]. The staggered (high PRF) ambiguous mode uses a sequence of M distinct PRIs that then repeat periodically. A mean PRF of the sequence is defined as the reciprocal of the sequence's mean PRI and is selected to be greater than the Doppler bandwidth.

It is worth noting the differences between the staggered ambiguous mode, shown in the right panel of Fig. 1, and the staggered SAR system in [27], [28], [29], [30], [31], [32], [33], [34], [35], [36], and [37] that employs DBF techniques, shown in the left panel of Fig. 1. The upper panel of Fig. 1 shows the simplified acquisition geometry for the staggered SAR system with DBF on the left and for the staggered ambiguous mode on the right. In both systems, a wide elevation transmit beam (not displayed in the figure) illuminates a wide swath and the echo corresponding to a given radiated pulse arrives back at the radar with increasing delays as the elevation angle (and therefore the slant range) increases. In the staggered SAR (the left panel of Fig. 1), however, DBF is used on receive to steer multiple narrow high-gain beam in real time toward the direction of arrival (DoA) of the radar echo from the ground, taking advantage of the one-to-one relationship between the radar pulse travel time and its DoA. In the staggered ambiguous SAR mode (the right panel of Fig. 1), instead, echoes are collected with the same wide beam used in transmit. The middle part of the left panel of Fig. 1 depicts the transmission and reception of radar echoes for the simplified case of a sequence of $M = 5$ PRIs. On the upper part of the middle panel, the transmitted pulses, separated by the varying PRIs, are displayed on a time axis. Ten pulses are transmitted, i.e., the PRI sequence is repeated twice. Each transmitted pulse is represented by different colors with the circled number indicating the pulse index. Immediately below, the received echoes corresponding to the first three transmitted pulses, i.e., those characterized by pulse indices 0, 1, and 2 are shown on the same time axis. The radar echoes from the sea clutter are displayed with the same colors as the corresponding transmitted pulses. The radar echo return from a ship at a slant range R_0 (for simplicity, we assume that the ship is not moving) overlaps to the echo return from the sea clutter and is marked in red with the upper circled number indicating the corresponding transmitted pulse. In this case, the radar echoes (from sea clutter and ship) for each transmitted pulse will be received by different receive beams, so the returns from the different pulses do not overlap. The echoes received by the different beams are then rearranged, i.e., shifted at the same reception time (see the bottom part of the left panel of Fig. 1), and the received radar echoes from the ship are at the same slant range R_0 for all range lines. Due to the radar's inability to receive while transmitting, some "blind areas" will be present on the received data with width equal to the pulse length plus the additional guard times that are necessary in the radar hardware to separate the pulse transmission from the receiving window. These "blind areas" are marked in black in the middle and last panels of Fig. 1. As the PRI is continuously varied, the locations of the blind areas will be different for each range line, as they are related to the time distances between the transmitted pulses.

In the staggered ambiguous mode of the right panel of Fig. 1, the receive echo window, EW, i.e., the time interval during which the receiver is turned on and can receive radar echoes, is typically much shorter than the duration of the radar echo from the illuminated swath

$$\mathrm{EW} \ll \frac{2(R_{\max} - R_{\min})}{c} \tag{1}$$

where c is the speed of light and $R_{\max}$ and $R_{\min}$ are the maximum and minimum slant ranges of the swath, respectively. As a result, preceding and succeeding echoes arrive at the radar at the same time as the desired return, resulting in range ambiguities. In the middle part of the right panel of Fig. 1, the same simplified case of a sequence of $M = 5$ PRIs is considered assuming transmission of ten pulses separated by varying PRIs. As before, the sea clutter returns are represented by different colors, corresponding to the transmitted pulses, and the ship return is marked in red. In this case, while we receive the desired radar echo of the ship at slant range R_0 from pulse number 0, marked in red with upper circled number 0, we will also receive an ambiguous return from pulse number 1, shown in white with upper circled number 1. This is also true for the sea clutter returns, which will overlap, as shown in the middle part of the right panel of Fig. 1. After rearranging the received echoes (see the bottom part of the right panel of Fig. 1), we have the radar echoes of the ship at the same slant range R_0 for all range lines as in the staggered SAR system, and we also have its ambiguous returns. Unlike in SAR modes with constant PRI, where range-ambiguous echoes of a scatterer appear at the same ranges along the entire synthetic aperture, range ambiguities in the staggered mode are located at different ranges for different range lines, as the time difference between the transmit pulses continuously varies. After SAR processing, the ambiguous energy is thus incoherently integrated and spread almost uniformly across the Doppler spectrum [29]. The same holds for sea clutter echoes; for example, we note in the middle part of the right panel of Fig. 1, the overlap caused by sea clutter returns from pulses 0, 1, and 2. This leads to an increase in the clutter level, which has to be accounted for within the assessment of the detection performance.

We have shown in [25] that the ambiguous SAR mode allows detecting small ships, i.e., of 21 m $\times$ 6 m size, with a probability of detection of 0.97 and 1000 false alarms per million of km^2, corresponding to a false alarm rate of 1.26×10^{-7}. The ambiguous mode therefore achieves a swath similar to that of a ScanSAR mode and a resolution cell of 2 m^2, similar to that of a spotlight mode. In [25], we showed that the probability of detection of a small ship in ScanSAR mode, which images the same 100-km swath with a coarser resolution of 5 m $\times$ 18.5 m (ground range $\times$ azimuth), would be less than 0.3, i.e., about 70% of the ships would be missed, assuming the same ship size and false alarms as in the ambiguous modes. High-resolution images are, in fact, characterized by more favorable ship statistics (higher mean values and standard deviation of the intensity in the focused

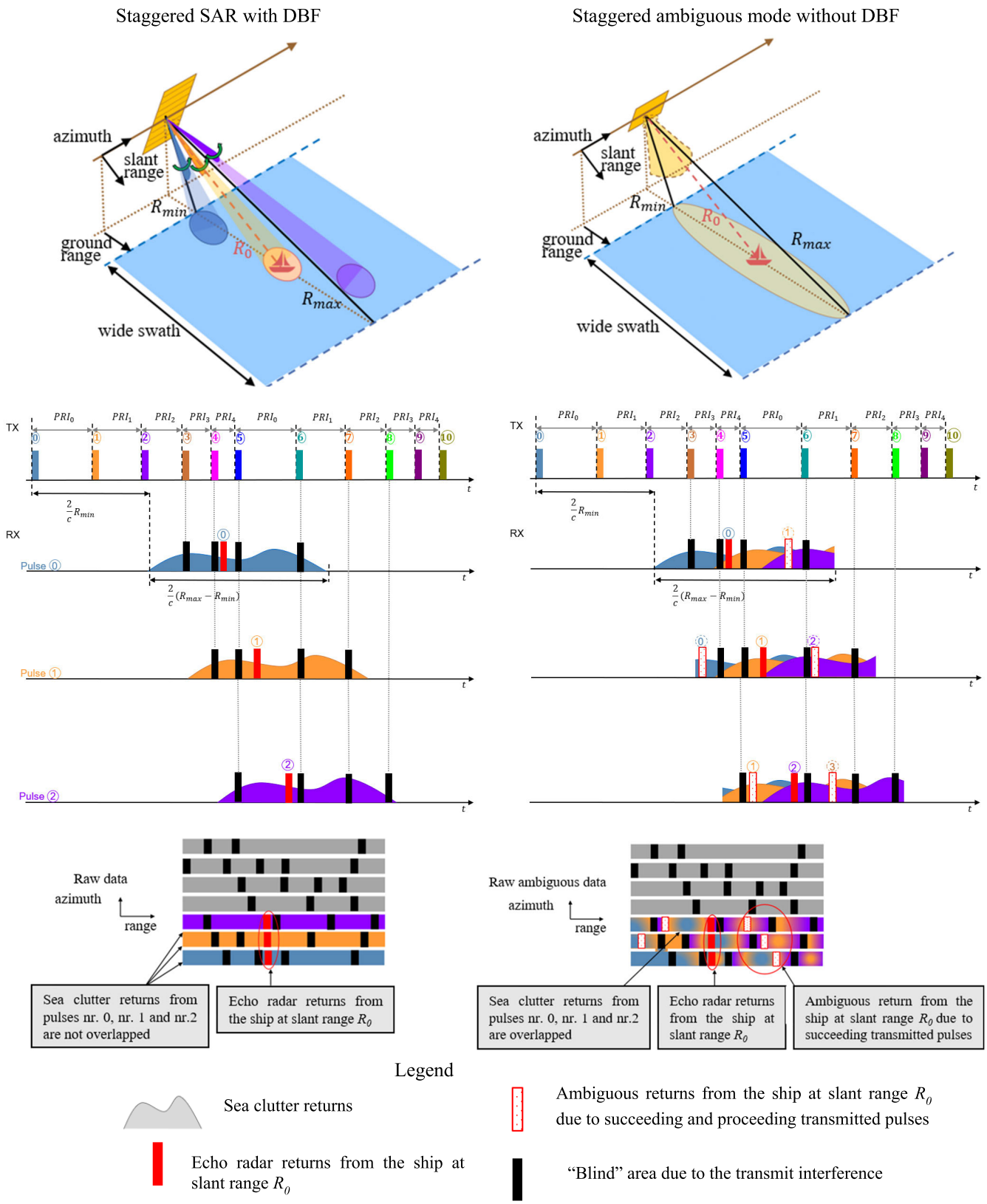

Fig. 1. Comparison between staggered SAR with DBF (left) and the staggered ambiguous mode without DBF (right). Top: simplified acquisition geometry (only the receiving beams are shown). Middle: transmitted pulses and corresponding received echoes. A sequence of $M = 5$ PRIs is assumed. Ten pulses are transmitted, i.e., the PRI sequence is repeated twice. The echoes from the sea clutter have the same colors as the corresponding transmitted pulses, the echoes from the ship at distance R_0 from the radar are marked in red and in white for the expected and ambiguous returns, respectively, and "blind" areas due to the transmit interference are marked in black. Bottom: raw data obtained by rearranging side by side the received echoes.

image), as discussed in [14], and more available pixels for the same ship size. The analysis shows that the effect of the higher resolution overcomes the increased level of background clutter and noise.

The idea of using an ambiguous mode (although the low PRF ambiguous mode in [25] and not the staggered ambiguous SAR one demonstrated in this article) has also been analyzed within the European Space Agency's (ESA) study "Persistent Responsive Real-Time Earth Observation (PERTEO)," whose goal is to provide real-time Earth Observation services to reduce natural disaster impact by proposing a heterogeneous small satellite constellation and performing in-orbit processing [38]. Preliminary analysis revealed that an efficient field-programmable gate array (FPGA) implementation for onboard processing from level 0 (raw data) to level 1 (complex focused SAR image) is feasible for a swath width of 90 km, a chirp bandwidth of 150 MHz, and an azimuth resolution of 1.7 m.

This article presents the design of an experimental TerraSAR-X acquisition using the high-resolution wide-swath staggered (high PRF) ambiguous mode for ship monitoring, the analysis of the expected performance, the processing of the data, and the validation of the results. This article is organized as follows. Section II describes how the TerraSAR-X technological limitations were tackled within the experiment design and discusses the expected performance for the planned acquisitions. Section III describes the processing of the acquired data, analyzes the resulting ambiguous SAR image, and discusses its interpretation with particular attention to the discrimination of range ambiguities. Section IV validates the detection results using maritime positioning data from the automatic identification system (AIS). Conclusions and perspectives are presented in Section V.

II. Design of the TerraSAR-X Experiment

TerraSAR-X is a versatile SAR satellite with several acquisition modes and a high level of operational flexibility. It has served the scientific community, as well as users from the commercial sector and government institutions, since its launch on June 15, 2007 [39]. TerraSAR-X is a conventional phased-array SAR that can be operated in staggered SAR mode because it has 512 different PRIs and can be commanded to transmit pulses based on a sequence of M distinct PRIs that then repeats periodically, as demonstrated in [29].

A. Parameter Selection

As a test site for the demonstration has been chosen an area in the North Sea not far from the German Bight. The imaged point closest to the coast has been selected to be approximately 27 km away from the Dutch coast, in order to avoid range ambiguities caused by strong land scatterers that could interfere with the ship detection. Note that ambiguous modes are not supposed to be used in coastal areas as the ambiguous returns from the land can impair the detection of ships; hence, an unambiguous mode, such as a conventional stripmap mode, should be used instead. Fig. 2 shows the test site; the red rectangle delimits the area of the acquired SAR image.

The selected elevation beam illuminates a 110-km ground swath with the minimum and maximum look angles of 53.74° and 56.67°, respectively. High incidence angles are selected because the sea clutter return is expected to be lower than at lower incidence angles. Moreover, the 110-km ground swath is not defined by the 3-dB antenna beamwidth, but by a beamwidth corresponding to about 8 dB below the maximum, as TerraSAR-X still provides adequate noise equivalent sigma zero (NESZ), i.e., adequate signal-to-noise ratio (SNR), to guarantee good ship detection performance over that larger swath, as discussed in Section II-B. We chose the horizontal transmit and horizontal receive (HH) polarization for this experiment because it is expected to lead to better detection performance [25].

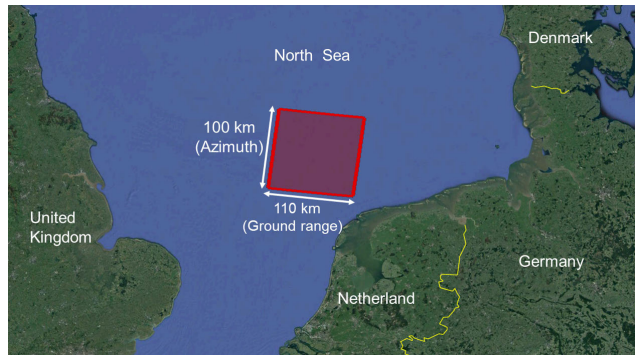

Fig. 2. North Sea test site near the German Bight selected for the experimental acquisition in staggered ambiguous mode. The red rectangle delimits the area of the acquired SAR image.

Once the beam has been selected, other system parameters, such as the PRI sequence, the pulse length τ, and the chirp bandwidth, must be chosen to ensure the best ship detection performance while respecting the TerraSAR-X technological constraints. We have shown in [25] that the best detection performance for an X-band system is obtained for the highest possible duty cycle value because it implies a better NESZ (or SNR), and for the highest selectable chirp bandwidth, because the effect of the improved resolution overcomes that of the reduced NESZ. The main TerraSAR-X parameters and constraints to be considered for the experiment are summarized in Table I.

One of the constraints is the maximum duty cycle $D_{\max}$ of 20%, defined as the ratio of the uncompressed pulse length τ to the PRI, which should hold for each distinct PRI and therefore also for the shortest $\mathrm{PRI}_{\min}$

$$\mathrm{PRI}_{\min} \geq \frac{\tau}{\mathrm{D}_{\max}}. \tag{2}$$

Another constraint is the maximum receive echo window length $\mathrm{EWL}_{\max}$, i.e., the maximum number of samples that can be memorized in the TerraSAR-X buffer, of 32 768 samples, which should hold for each distinct PRI and therefore also for the longest $\mathrm{PRI}_{\max}$

$$\mathrm{PRI}_{\max} \leq \frac{\mathrm{EWL}_{\max}}{F_r} + \tau + \tau_{\mathrm{RX-TX}} + \tau_{\mathrm{TX-RX}} \tag{3}$$

where $\tau_{\mathrm{RX-TX}}$ and $\tau_{\mathrm{TX-RX}}$ are the time guards between receive and transmit and transmit and receive, respectively (see Table I), and F_r is the sampling frequency that for TerraSAR-X is approximately 10% higher than the selected chirp bandwidth B_r.

TABLE I
MAIN TERRASAR-X PARAMETERS AND CONSTRAINTS TO BE CONSIDERED FOR THE EXPERIMENT

Parameter	Symbol	Value
Radar wavelength	λ	0.0311 m
Orbit height	h	515 km
Antenna type		Planar
Antenna length	L_a	4.8 m
Antenna width	W_a	0.7 m
Maximum duty cycle	D_{max}	20%
Maximum echo window length	EWL_{max}	32768 samples
Maximum pulse length	τ_{max}	67 µs
Minimum pulse length	τ_{min}	15 µs
Time guard between receive and transmit	τ_{RX-TX}	5.2 µs
Time guard between transmit and receive	τ_{TX-RX}	3.271 µs
Sampling frequency	F_r	1.1×B_r
Minimum selectable pulse repetition frequency	$PRF_{min_{TS-X}}$	1999.96 Hz
Maximum selectable pulse repetition frequency	$PRF_{max_{TS-X}}$	6706.91 Hz

A chirp bandwidth of 300 MHz, the highest available in TerraSAR-X, which allows for the highest range resolution, cannot be chosen for this experiment. The maximum duty cycle constraint of (2), in fact, requires $\tau < 41.3$ μs. By substituting the values of the maximum echo window length and the guard times from Table I in (3), it turns out that for values of $\tau < 41.3$ μs, $\mathrm{PRI}_{\max}$ is smaller than the minimum selectable PRI value for TerraSAR-X, i.e., 0.1491 ms. While for a 150-MHz chirp bandwidth, it is possible to find a sequence of PRIs that satisfies both constraints (2) and (3) for a pulse length of 30 μs, the data rate from the instrument buffer to the mass memory imposes a further limitation on the chirp bandwidth for such a large swath. A chirp bandwidth of 100 MHz has therefore been chosen for this experiment, resulting in a ground range resolution at near range, $R_{\min}$, of 1.72 m, if no windows are used within the processing. For a pulse length of 45 μs, is it possible to design a sequence of $M = 43$ PRIs (selected among the 512 available PRIs) that satisfies both constraints in (2) and (3) and follows an almost linear decreasing trend. Fig. 3 shows the chosen PRI sequence as a function of the pulse index. The mean PRF of sequence, which is the reciprocal of the mean PRI, is $\mathrm{PRF}_{\mathrm{mean}} = 3525$ Hz, which is greater than the 3-dB (one-way) Doppler bandwidth of the system, $B_{\mathrm{Dop}} = 2807$ Hz. The average duty cycle of the sequence is 16.1%. Table II reports the selected parameters for the experiment, including the processing parameters.

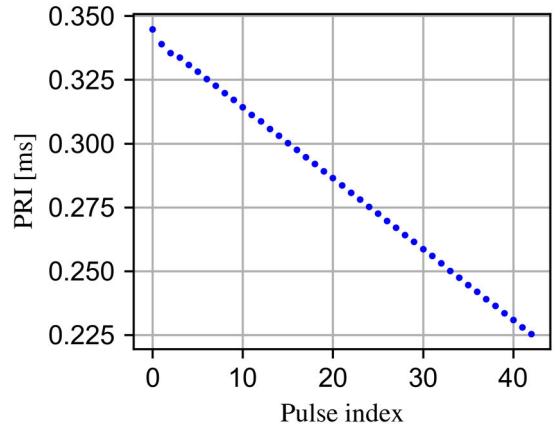

Fig. 3. Selected PRI sequence as a function of the pulse index.

TABLE II
SELECTED PARAMETERS FOR THE EXPERIMENT

Parameter	Symbol	Value
Wave polarization		HH
Minimum slant range	R_{min}	948.7 km
Maximum slant range	R_{max}	1047.1 km
Chirp bandwidth	B_r	100 MHz
Pulse length	τ	45 µs
Mean PRF	PRF_{mean}	3525 Hz
Processed Doppler bandwidth	PBW	2807 Hz
Azimuth weighting window		No
Compensation of the azimuth antenna pattern		No
Range weighting window		No
Resampling method for the nonuniform data		Two-point linear interpolation on raw data

The location of the missing samples (i.e., blind areas) in the raw data for one cycle of the selected PRI sequence is shown in Fig. 4 (i.e., areas in black) using the blockage diagram approach as in [40]. Because TerraSAR-X has a limited number of selectable PRFs, the condition that two consecutive azimuth samples are never missed [28], as shown by the two red arrows in Fig. 4, is not satisfied for each range line for the selected PRI sequence. This usually allows for more accurate interpolation of nonuniformly sampled raw data on a uniform grid and lower azimuth ambiguity-to-signal ratio (AASR) but is not a strict requirement and can be tolerated for this mode, where range ambiguities dominate over azimuth ambiguities.

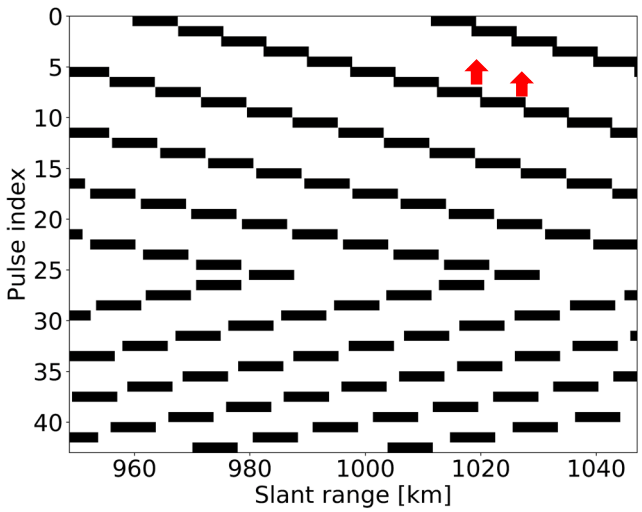

Fig. 4. Location of the missing samples in the raw data (areas in black, where the echo cannot be recorded, as the radar is transmitting) for the imaged 98.3-km swath in slant range (110-km ground range swath).

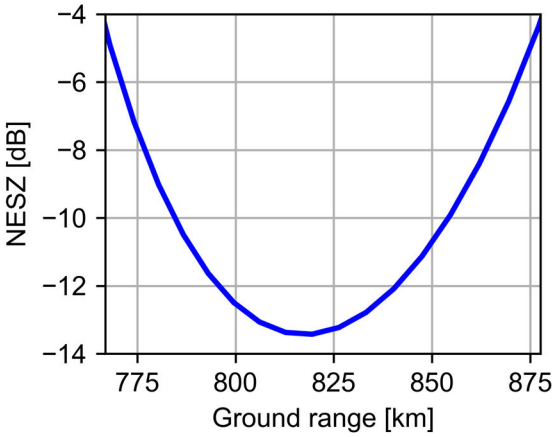

Fig. 5. NESZ as a function of the ground range for the selected antenna beam and the parameters of Table II.

B. Expected Performance

The detection performance ultimately depends on the ship size and the statistics of the background disturbance, which includes the thermal noise and the sea clutter. Furthermore, the specific ambiguous mode requires careful consideration of the effects of ambiguities of both the sea clutter, which might be significantly amplified, and the ships, which might result in false alarms.

As for the thermal noise, the NESZ is evaluated for the selected antenna beam and shown as a function of ground range in Fig. 5. The NESZ ranges from −14 dB at the swath center to about −4 dB at near and far range and is much worse than for typical TerraSAR-X stripmap acquisitions.

In the staggered ambiguous mode, the sea clutter component consists of an unambiguous component from the main lobe and the ambiguous sea clutter components resulting from both range and azimuth ambiguities. According to the definition of the ambiguity-to-signal ratio (ASR), i.e., the ratio between the power of the ambiguous signal and the power of the main signal, the total sea clutter in the staggered ambiguous mode

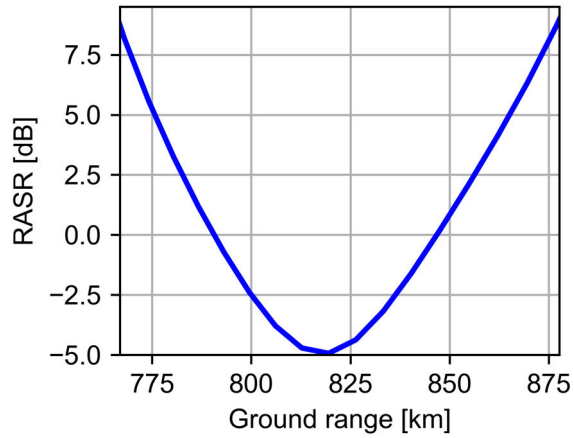

Fig. 6. RASR as a function of the ground range for the selected antenna beam and the parameters of Table II.

is equal to the sea clutter of the unambiguous component multiplied by one plus the ASR of the system. This amplification occurs because the unambiguous sea clutter component and the ambiguous sea clutter components are independent of each other, as they originate from different areas.

Under the assumption that the backscatter return has a constant trend over range and that no amplitude weighting in azimuth is performed, we can approximate the range ambiguity-to-signal-ratio (RASR) in [29] and [30] as

$$\mathrm{RASR} \approx \frac{\frac{1}{M}\sum_{m=0}^{M-1}\sum_{j=1}^{N_{A_m}} \frac{\frac{1}{\mathrm{PRF}_{\mathrm{mean}}} G^2(\theta_{jm})}{R_{jm}^3 \sin\eta_{jm}}}{\frac{\frac{G^2(\theta_{\mathrm{main}})}{\mathrm{PRF}_{\mathrm{mean}}}}{R_{\mathrm{main}}^3 \sin\eta_{\mathrm{main}}}} \tag{4}$$

where $G^2(\theta)$ is the two-way antenna pattern in elevation as a function of the elevation angle, R denotes the slant range, η denotes the incidence angle, and the subscript m, $m = 0, \ldots, M-1$, refers to the transmitted pulse of the sequence and j, $j = 1, \ldots, N_{A_m}$, to the N_{A_m} ambiguous (preceding and succeeding) returns, while the subscript "main" refers to the desired return. The RASR is shown in Fig. 6 as a function of the ground range for the PRI sequence in Fig. 3 and the parameters of Table II and ranges from −4.8 dB at the swath center to 8.8 dB at the far range.

The AASR for a variable PRI SAR is also evaluated following the approach in [29] and [30], i.e., as the difference of the integrated sidelobe ratios and is in the order of −11.5 dB, therefore negligible compared to the RASR. Therefore, we can approximate the total sea clutter as the sea clutter of the unambiguous component multiplied by one plus the RASR.

The backscatter level of the sea clutter depends on the condition of the sea. Typical mean values of the backscatter in the X-band for calm sea range between −16 and −18 dB, but a more conservative value of −14 dB could also be considered to account for the increase of backscatter due to wind. Fig. 7 shows the total background disturbance, i.e., total sea clutter plus thermal noise, for backscatter levels of the sea clutter of −14, −16, and −18 dB.

Finally, the probability of detection of a small ship of 21 m × 6 m size is evaluated using the closed-form expression in [14] and [25] for 1000 false alarms per million of km^2,

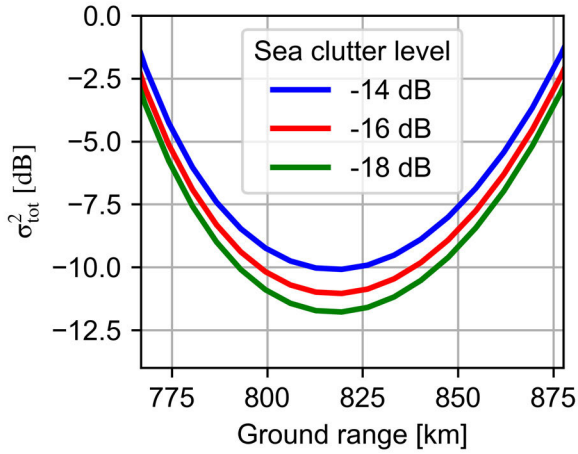

Fig. 7. Total disturbance as a function of ground range for the selected antenna beam and the parameters of Table II.

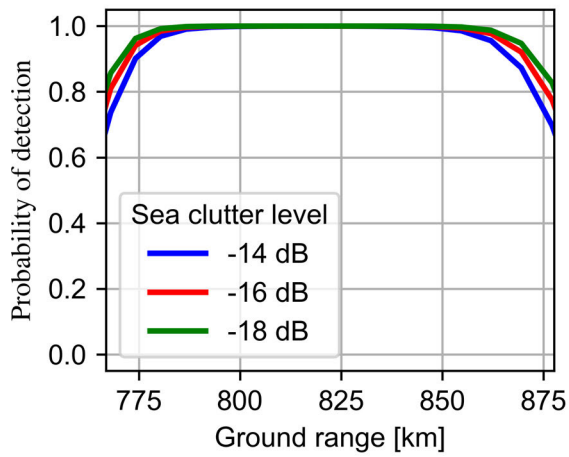

Fig. 8. Probability of detection of a small ship of 21 m × 6 m size as a function of ground range for 1000 false alarms per million of km^2, corresponding to a false alarm rate of 1.26×10^{-7} and different backscatter levels of the sea clutter.

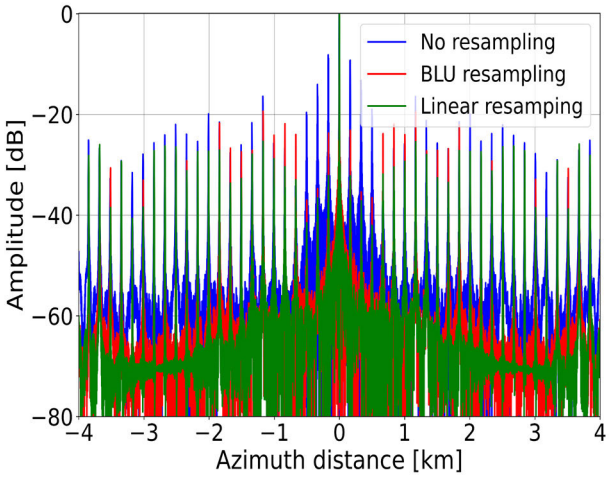

Fig. 9. 1-D (azimuth) IRF for a slant range $R_0 = 998$ km obtained by the 1-D simulation using the sequence of $M = 43$ PRIs of Fig. 3 and the system parameters of Table II.

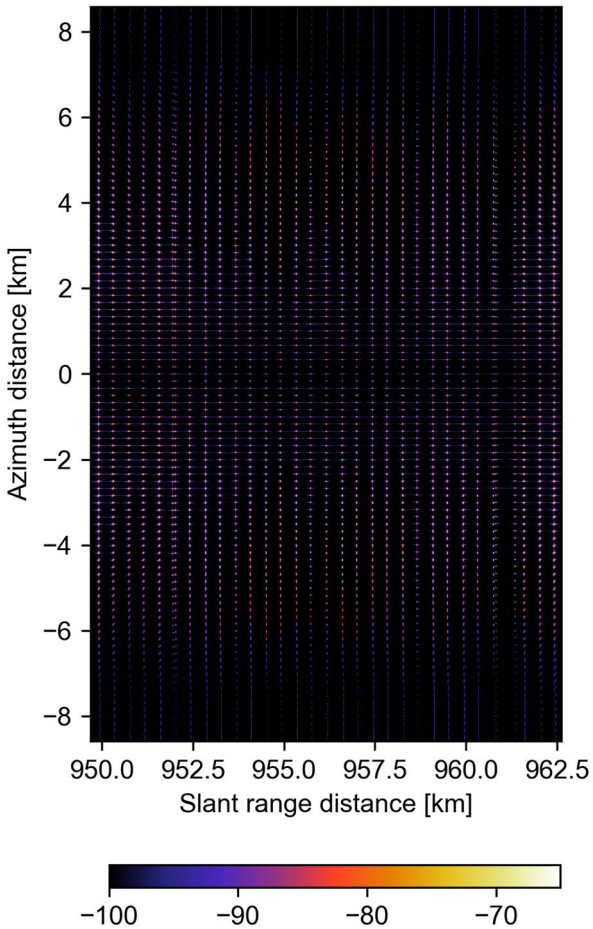

Fig. 10. 2-D IRF of the first-order range-ambiguous point scatterer obtained by the 2-D simulation using the sequence of M= 43 PRIs of Fig. 3 and the system parameters of Table II. The peak value is −30 dB.

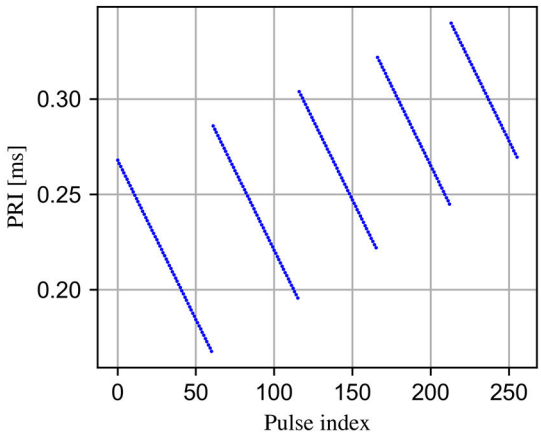

Fig. 11. More elaborated PRI sequence (M= 256) consisting of five sequences with fast PRI variation concatenated as a function of the pulse index. The mean PRF of the sequence is $\mathrm{PRF}_{\mathrm{mean}} = 3972$ Hz.

corresponding to a false alarm rate of 1.26×10^{-7}, the total disturbance of Fig. 7, and an azimuth resolution of 2.2 m. The probability of detection is shown in Fig. 8 as a function of ground range for different backscatter levels of the sea clutter. Due to the variable PRI operation, which results in an incoherent integration of the ambiguous echoes appearing at different

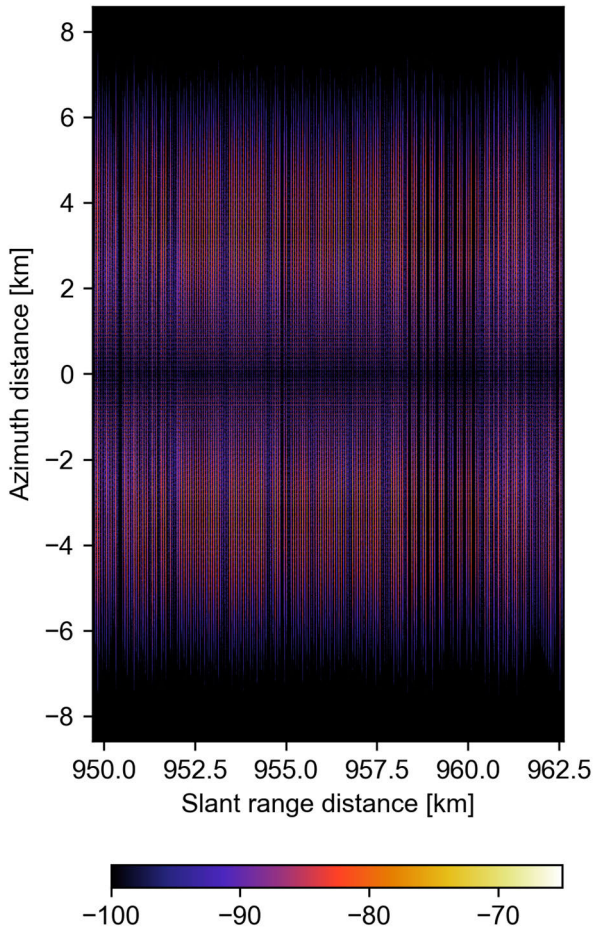

Fig. 12. 2-D IRF of the first-order range-ambiguous point scatterer obtained by the 2-D simulation using the sequence of M= 256 PRIs of Fig. 11 and the system parameters of Table II. The peak value is −45 dB.

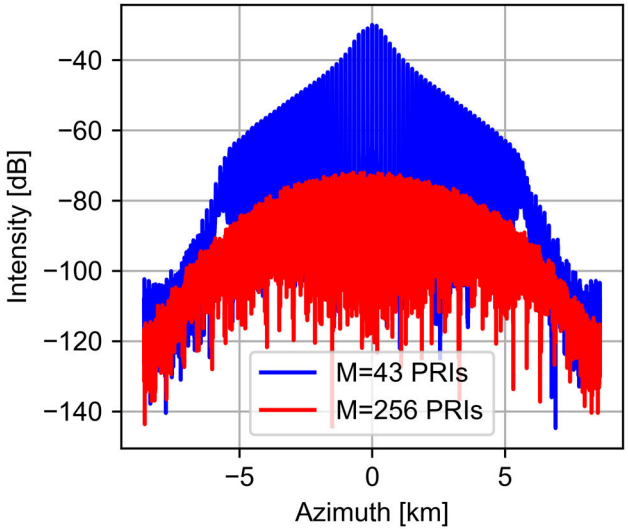

Fig. 13. Comparison of the cut along azimuth at $R = 958$ km between the 2-D IRF of the first-order range ambiguity for the sequence of $M = 43$ PRIs used in the experiment and the sequence of $M = 256$ PRIs of Fig. 11.

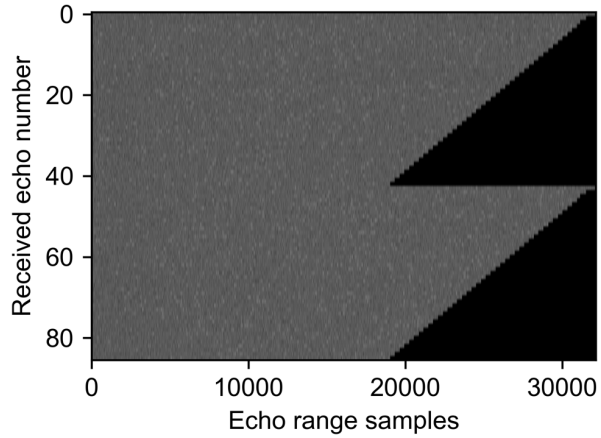

Fig. 14. 86 echoes received between consecutive transmitted pulses. The horizontal axis represents the fast time.

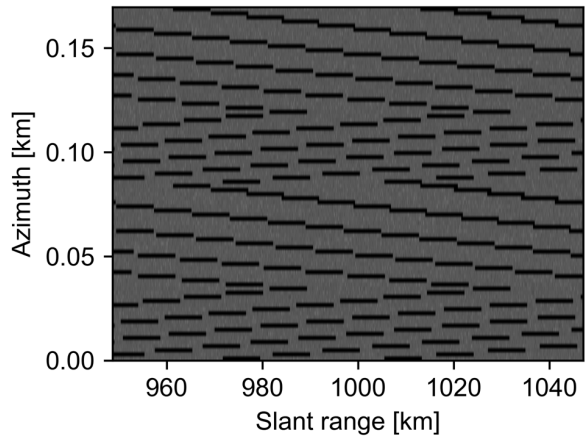

Fig. 15. 86 range lines obtained after rearranging the echoes of Fig. 14. The horizontal axis represents the slant range (98.4 km) and the vertical axis represents azimuth (0.17 km).

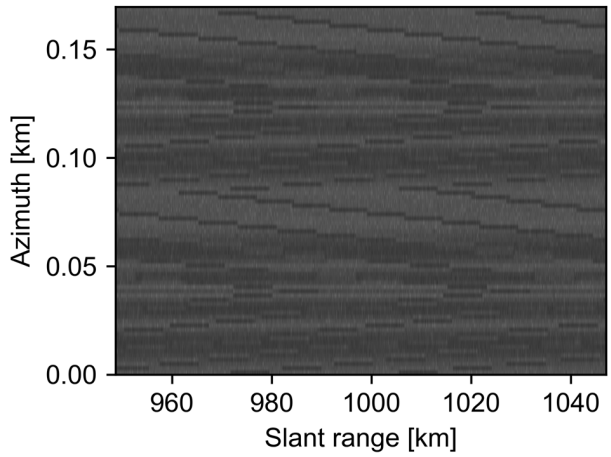

Fig. 16. Resampled data (86 lines) using two-point linear interpolation. The horizontal axis represents the slant range (98.4 km) and the vertical axis represents azimuth (0.17 km).

ranges, the disturbance resulting from the ambiguous clutter can be considered as noise-like. The achieved probability of detection is always better than 0.5 for a backscatter level of the sea clutter of −14 dB.

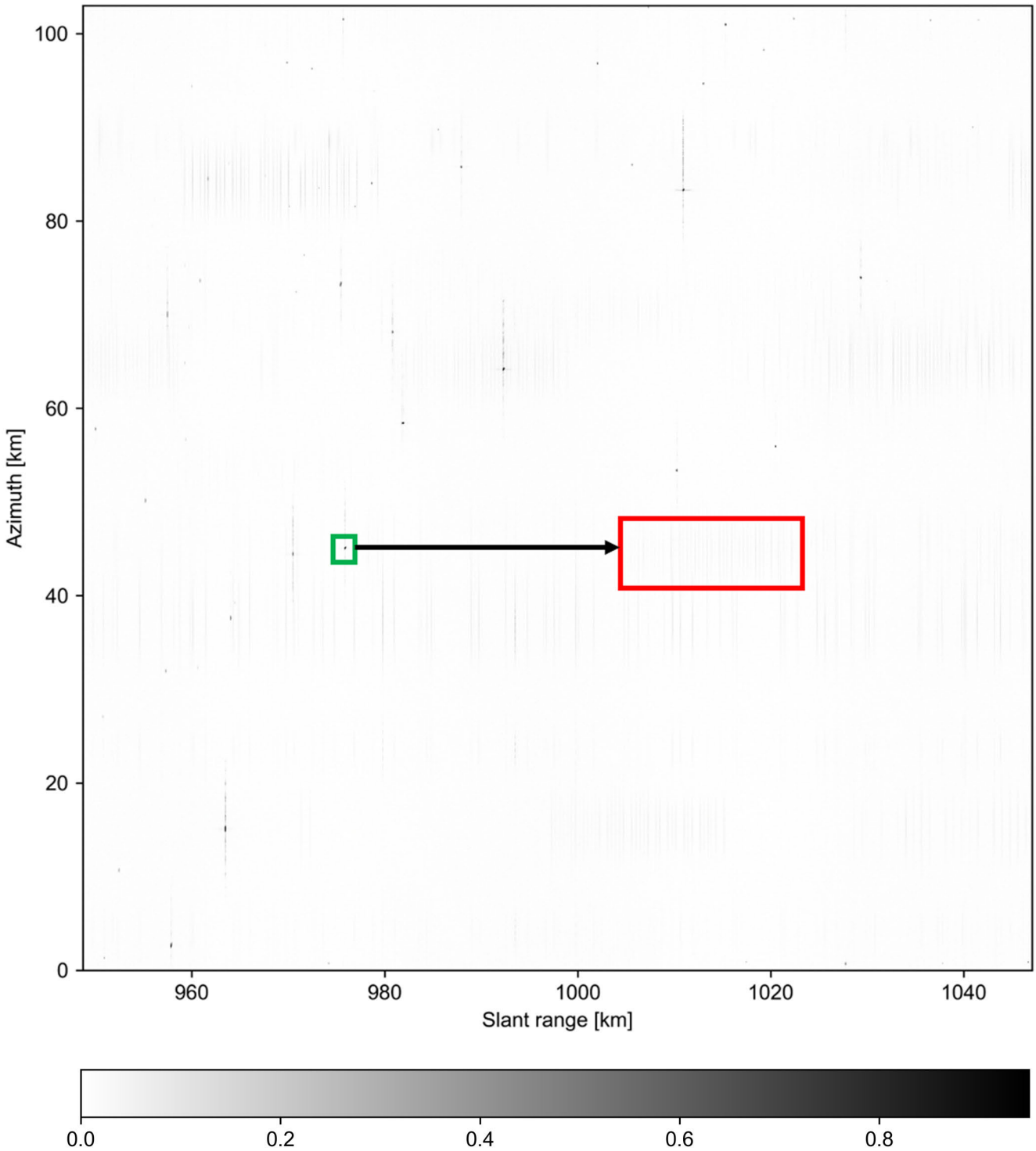

Fig. 17. Intensity of the focused image acquired by TerraSAR-X in staggered ambiguous mode over the full scene. The green rectangle highlights one of the large ships in the scene and its sidelobes, and the red rectangle highlights a part of the image affected by the first-order range ambiguity of the ship in the green rectangle.

The performance of Fig. 8 does not account for the false alarms due to the ambiguities of ships. In order to understand this aspect more in depth, it is worth observing the signatures of both azimuth and range ambiguities for the specific mode and system parameters.

The 1-D azimuth impulse response function (IRF) for a slant range $R_0 = 998$ km (the swath center) is shown in Fig. 9 for different resampling options [no resampling, two-point linear interpolation, and best linear unbiased (BLU) interpolation] [29], [30]. It can be noticed that the grating lobes due to azimuth ambiguities are lower for linear interpolation (green curve) than for the BLU interpolation (red curve), as the azimuth oversampling is limited. Two-point linear interpolation is therefore used to process the data. The 1-D IRF

of the nonresampled data (blue curve), obtained by focusing the data as if they were acquired with a constant PRF equal to the mean PRF of the sequence, has much higher grating lobes than the resampled data and should therefore be considered as an option only if fast processing is required and the resources are limited, e.g., for onboard near real-time processing.

The 2-D IRF of the first-order range ambiguity for a point scatterer is shown in Fig. 10. As the PRIs available in TerraSAR-X do not allow for a finer PRI variation, the range ambiguity of a point scatterer appears as a set of lines parallel to the azimuth direction.

A finer PRI variation, e.g., using the more elaborated PRI sequences in [27], would smear the range ambiguities in the range direction as well, making them appear as a noise-like disturbance. Fig. 11 shows more elaborated PRI sequences with finer PRI variation. Specifically, five sequences of PRI ($M = 256$) with fast PRI variation are concatenated. Fig. 12 shows the 2-D IRF of the first-order range ambiguity for a point scatterer, using the aforementioned elaborated PRI sequence. We note that in this case, the ambiguous energy of a point scatterer not only smears along azimuth but also in range due to the finer PRI variation. Furthermore, through the comparison of the range cuts shown in Fig. 13, we observe a decreased intensity level of the range ambiguities when using a PRI sequence with finer PRI. This observation serves as further confirmation that the presence of range ambiguities from ships will not have an impact on ship detection. In scenarios involving highly congested sea traffic situated far from the coast, the use of the staggered ambiguous SAR with more elaborated PRI sequence becomes a viable option.

This is due to the possibility of detecting small ships even when overlapped with the smeared range ambiguities of large ships. Specifically, a higher detection threshold can be applied in the regions where this overlap occurs, facilitating the successful detection of small ships.

III. Data Processing

The TerraSAR-X experimental acquisition in staggered ambiguous mode has been performed on July 11, 2022, over the North Sea. The sequence of 43 PRIs in Fig. 3 is repeated 1200 times. The echoes, received by the radar between consecutive transmitted pulses, have different durations, as different PRIs are employed. Fig. 14 shows 86 consecutive received echoes, i.e., two cycles of PRI sequence, where the decreasing length of the radar echoes over a cycle of 43 transmitted pulses is visible. Unlike in an SAR with constant PRI, the first samples of the received echoes correspond in a staggered SAR system to different slant ranges. Those echoes have therefore to be rearranged in a 2-D matrix with coordinates slant range and azimuth, associating each sample of the radar echo to the corresponding range as described in Section I. Fig. 15 shows the rearranged echoes of the 86 echoes of Fig. 14, where the missing samples due to the transmit interference are visible and follows the pattern of missing samples provided in the diagram of Fig. 4. Please note that each received echo contains not only the desired return but also the returns of preceding and succeeding pulses as they arrive back at the radar at the same time. Raw data with gaps have then to be resampled to a uniformly spaced grid. Fig. 16 shows 86 range lines of the resampled data, obtained using two-point linear interpolation.

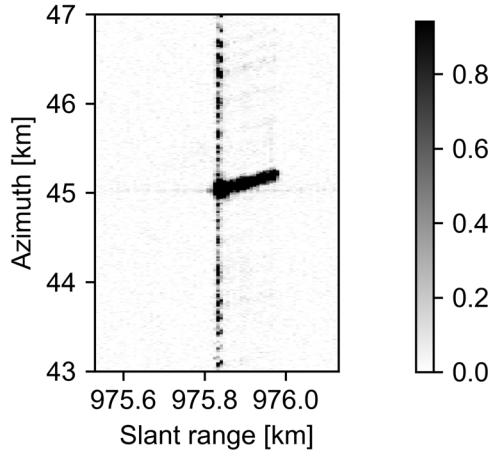

Fig. 18. Zoom around the large ship and its sidelobes highlighted by the green rectangle in Fig. 17.

The resampled raw data can then be focused using the approximated Omega-K algorithm [41]. It is worth noting that other focusing algorithms can also be employed following the resampling of the raw data onto a uniform grid. Fig. 17 shows the intensity of the focused data for the full scene of over 10 000 km^2, where the strong returns of the ships can be observed. Fig. 18 shows a zoom around one of the large ships in the scene, for which the response extends in azimuth due to the presence of azimuth ambiguities. In addition to the ships, the range ambiguities of the ships are visible as sets of equally spaced lines parallel to the azimuth directions. Fig. 19(a) shows a zoom around the first-order range ambiguity of the large ship of Fig. 18 that has a signature similar to the 2-D IRF of the first-order range ambiguity shown in Fig. 10.

If an automated detection algorithm based on a threshold, such as the one discussed in [14], were applied to the data, numerous false alarms would appear due to the ambiguities of the ships. Range ambiguities would, however, be no issue, if a finer PRI variation could be employed. In that case, in fact, their level would be well below the detection threshold. For instance, in Fig. 19(b), the first-order range ambiguity of the large ship in Fig. 18 is shown as if it were obtained using a more elaborate PRI sequence, as shown in Fig. 11. The sea clutter is overlapped with the range ambiguity. We observe that, in this case, the range ambiguity of the ship remains below the sea clutter level and is not visible, differently from Fig. 19(a). Furthermore, we have observed that the range ambiguity of the ship does not exceed the threshold computed as described in [14].

In our case, where the radar is limited in the selection of the PRIs, the range ambiguities of the ships can be identified based on their specific signature and expected distance from the ship, as highlighted by the green and red rectangles in Fig. 17.

The specific signature of range ambiguity might even allow detecting and locating (large) ships outside the imaged swath, as long as sufficient power is received, e.g., through the

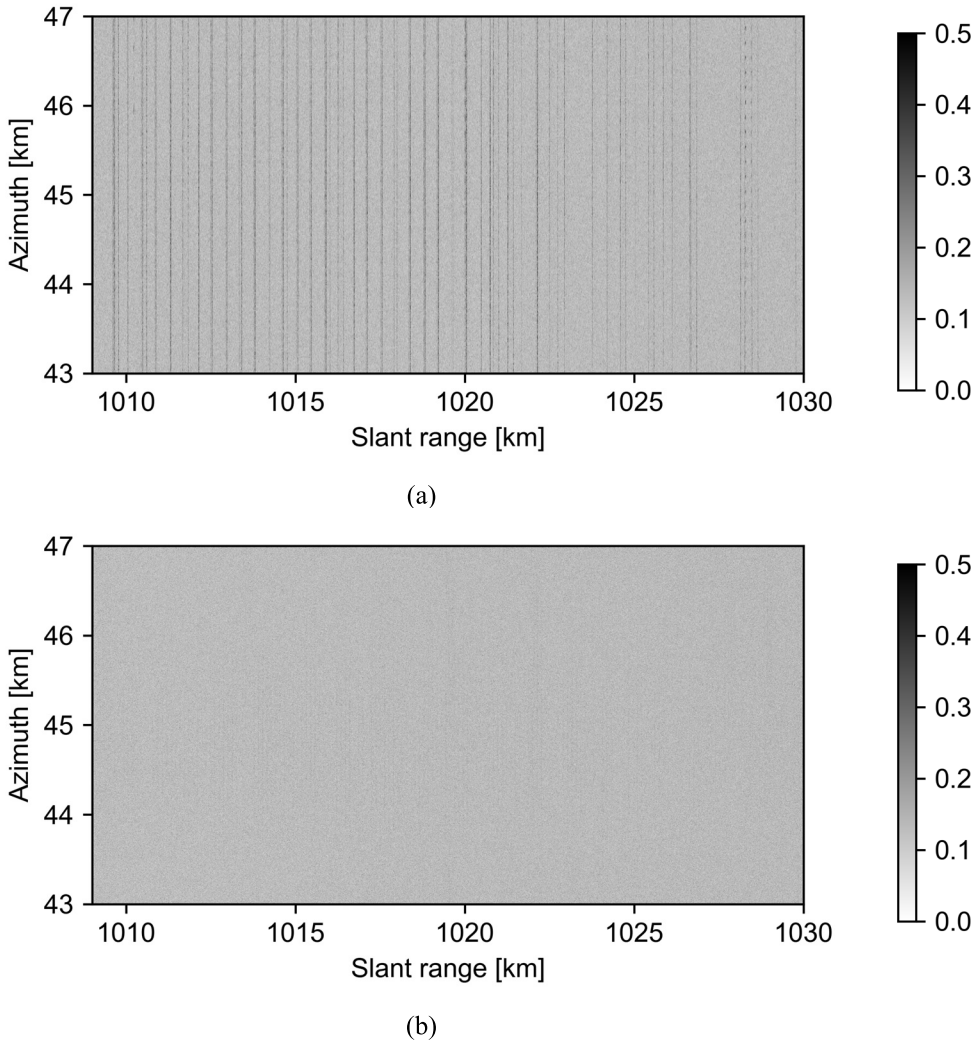

Fig. 19. (a) Zoom around the first-order range ambiguity of the large ship highlighted by the red rectangle in Fig. 17. (b) First-order range ambiguity of the large ship in Fig. 18 as if obtained with the more elaborated sequence of $M = 256$ shown in Fig. 11. Note that the color scale differs from that in Figs. 17 and 18 to better emphasize the range ambiguities.

sidelobes. In case a finer PRI variation cannot be employed, an empirical additional threshold can be used to discriminate range ambiguities. For the settings of this experiment, a second threshold about 3 dB above the detection threshold has proved to be effective to remove range ambiguities and having all unambiguous returns from ships exceed it.

A total of 57 ships have been detected in the full scene, namely, ten small ships (ship length $\leq$ 25 m), 25 medium ships (25 m $<$ ship length $\leq$ 150 m), and 22 large ships (ship length $>$ 150 m).

IV. Validation With Ground Truth From AIS Data

The International Convention for the Safety of Life at Sea requires AIS transponders to be carried on all ships exceeding 300 tons engaged in international voyages, cargo ships of 500 tons and above not engaged in international voyages, and all passenger ships [42]. Communication losses in AIS systems can occur due to physical limitations of their components, such as very high-frequency propagation losses or multipath signal reception effects. As a result, combining SAR and AIS data results in more effective ship monitoring by allowing the identification of illegal vessels that lack an AIS or vessels that do not broadcast AIS messages for technical reasons. The Maritime Security Lab at DLR's German Remote Sensing Data Center in Neustrelitz, Germany, has developed a possible approach for SAR-AIS data fusion for near real-time applications related to maritime situational awareness [42], [43], [44].

Two different AIS datasets provided by VesselFinder Limited [45] and MarineTraffic [46] have been used as ground truth to validate the effectiveness of the staggered ambiguous mode for ship monitoring. The AIS data from both datasets have been extracted within the same time interval of 30 min, starting 15 min before the start of the TerraSAR-X acquisition, which takes about 15 s. The 247 positions associated with 13 ships were provided by VesselFinder Limited, whereas 53 positions associated with 12 ships were provided by MarineTraffic. It is important to note that AIS transponders broadcast the position of the vessel at various time intervals ranging from 2 s for fast moving targets to 3 min for anchored

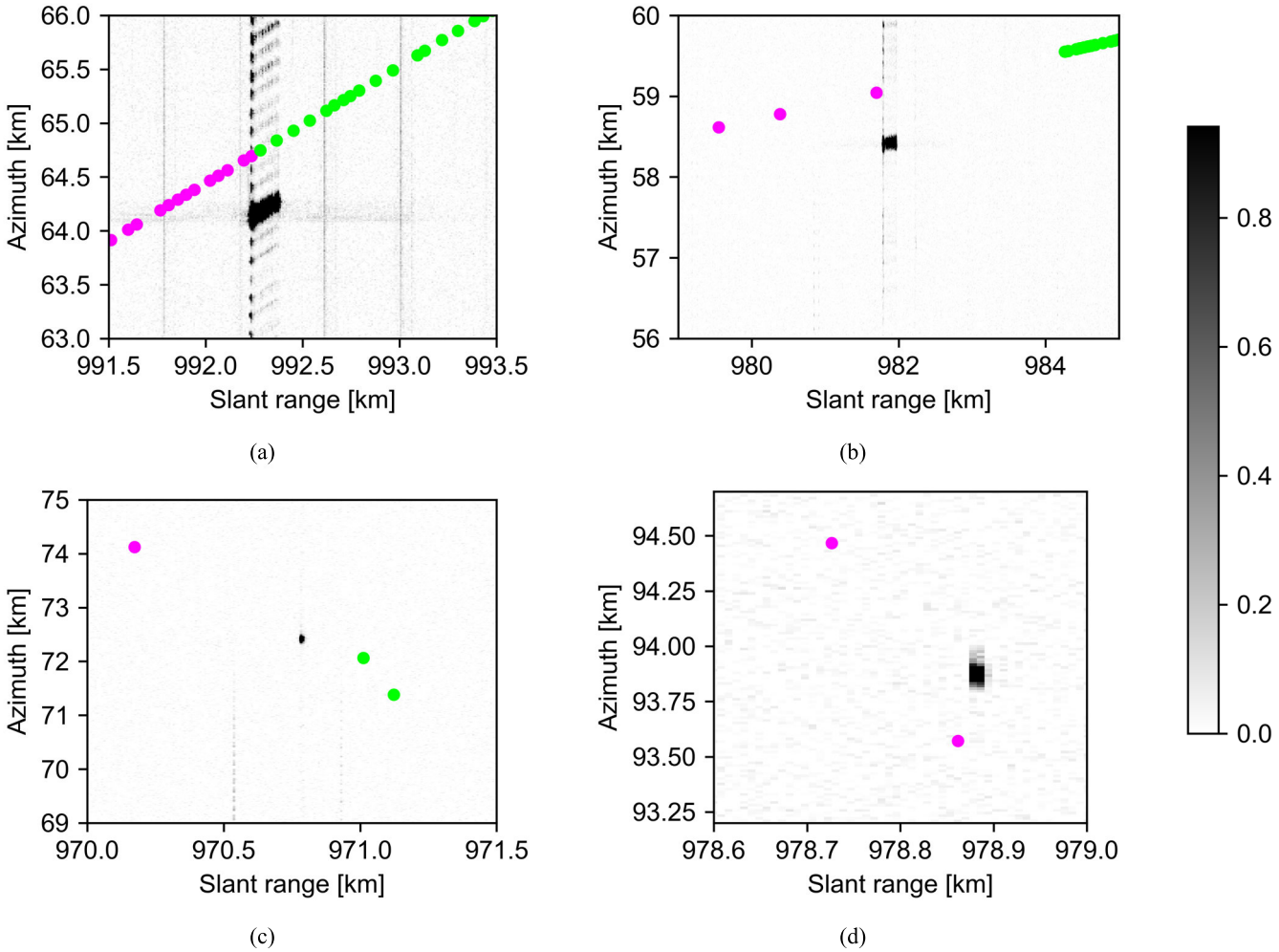

Fig. 20. AIS tracks (green and purple points) overlaid to portions of the SAR image of Fig. 17 with ships. The purple and green portions of the AIS tracks correspond to the AIS points before and after the SAR acquisition, respectively. (a) Large ship of 229 m × 35 m size with a radial velocity of 4.26 m/s and azimuth shift of 556 m. (b) Large ship of 229 m × 32 m size with a radial velocity of 5.3 m/s and azimuth shift of 679 m. (c) Fishing vessel of 28 m × 6 m size with radial velocity of 1.15 m/s and azimuth shift of 192 m. (d) Fishing vessel of 24 m × 7 m size with radial velocity of 0.16 m/s and azimuth shift of 21 m.

vessels. Moreover, in some cases, such as deliberate partial switching of the AIS transponder or surveillance of areas beyond the reception range of terrestrial antennas, the time interval between receiving two AIS positions can be even longer than three minutes. Each individual vessel is identified by its Maritime Mobile Service Identity number (MMSI). Comparing the MMSI of the two datasets, we noticed that 11 ships are present in both datasets, while one ship is present only in the MarineTraffic dataset and two ships are present only in the VesselFinder Limited dataset. AIS specifications for the vessel's size and type are not included in the MarineTraffic dataset, whereas the VesselFinder Limited dataset has this information for 8 out of 13 ships. Four of the eight ships are fishing vessels, with the smallest being 24 m × 7 m size, three ships are classified as cargo, and the largest ship is a tanker of 274 m × 48 m size.

AIS tracks have been projected into the focused SAR image of Fig. 17. Zooms around four of the detected ships are shown in Fig. 20, where the AIS points before and after the SAR acquisition are marked with distinct colors (purple and green, respectively). The ships in Fig. 20(a) and (b) are large ships of 229 m × 35 m size and 229 m × 32 m size, respectively, whereas the ships in Fig. 20(c) and (d) are fishing vessels of 28 m × 6 m size and 24 m × 7 m size, respectively. It can be noticed that while the slant range position is consistent between the AIS and the SAR data, an azimuth shift appears.

This is due to the so-called "train-off-the-track effect," i.e., the fact that a moving target induces an additional Doppler shift beyond that of a stationary target. Moving targets in focused SAR images therefore appear displaced in the azimuth direction from their actual geographical position by [46]

$$\Delta_{\mathrm{az}} = \frac{R_0 v_{r\mathrm{ship}}}{v_s} \tag{5}$$

where R_0 is the ship slant range, $v_{r\mathrm{ship}}$ is the radial velocity of the ship, and v_s is the satellite velocity. The azimuth shifts for the four ships of Fig. 20 correspond to the theoretical value calculated from (5). Table III compares the radial velocity retrieved from AIS data to the radial velocity estimated from

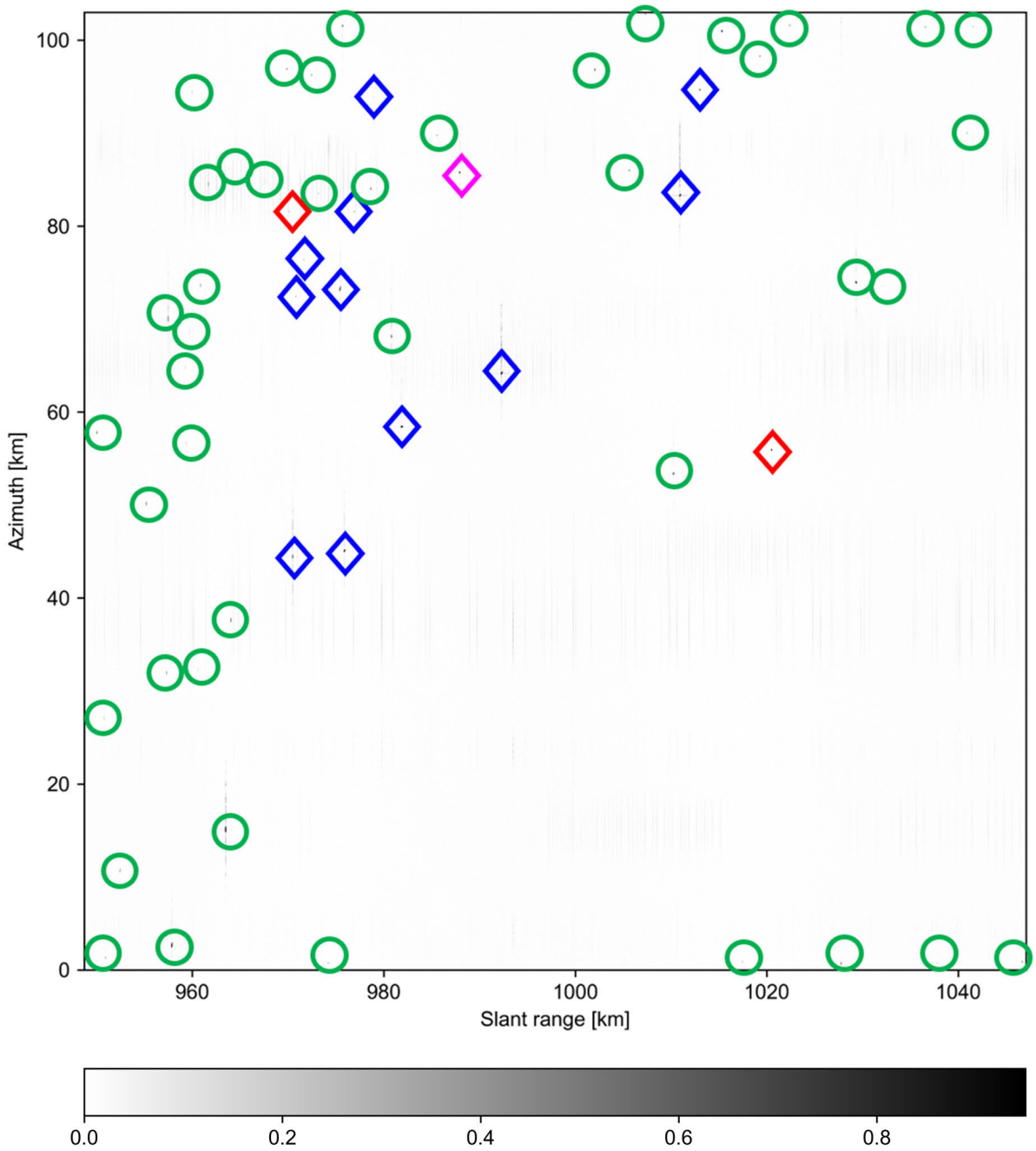

Fig. 21. Intensity of the focused image acquired by TerraSAR-X in staggered ambiguous mode over the full scene with superimposed the detected ships. Blue diamond markers highlight the 12 detected ships that are presented in both AIS datasets, red diamond markers highlight the two detected ships that are present only in the VesselFinder Limited dataset, magenta diamond marker highlights the one detected ship presented only in the MarineTraffic dataset, and the green circle markers highlight the remaining 43 detected ships without AIS.

the azimuth shift observed on the SAR image compared to the AIS positions for the four ships shown in Fig. 20, and we note a good agreement between the results. It is important to note that the derived radial velocity from the azimuthal shift yields more accurate results for the two larger ships due to the availability of a greater number of AIS positions compared to the small ships.

All ships that are present in both AIS datasets are correctly associated with the detected ships on the SAR image. The comparison of the positions of the ships provided by the AIS and the estimated position from the geocoded SAR image showed that the localization accuracy is in the order of 10 m and therefore allows in most cases for a correct association of the detected ships in SAR data with the corresponding AIS entry.

In Fig. 21, the 12 detected ships presented in both AIS datasets are shown with blue diamond markers; the 2 ships present only in the VesselFinder Limited dataset are indicated with red diamond markers; the ship present only in the MarineTraffic dataset is marked with a magenta diamond;

TABLE III
COMPARISON BETWEEN THE RADIAL VELOCITY RETRIEVED FROM THE AIS DATA AND THE RADIAL VELOCITY ESTIMATED FROM THE AZIMUTH SHIFT OBSERVED ON THE SAR IMAGE COMPARED TO AIS POSITIONS

Ship	Radial velocity retrieved from the AIS data	Radial velocity estimated from the SAR image
Large ship of 229 m × 35 m	4.26 m/s	4.02 m/s
Large ship of 229 m × 32 m	5.26 m/s	5.2 m/s
Small ship of 28 m × 6 m	1.51 m/s	1.56 m/s
Small ship of 24 m × 7 m	0.16 m/s	0.28 m/s

and the 43 detected ships only in the TerraSAR-X image are represented with green circle markers.

V. CONCLUSION AND PERSPECTIVES

An experimental TerraSAR-X acquisition in staggered ambiguous mode imaging a ground swath of 110 km with 2.2-m azimuth resolution has been performed over the North Sea. Data have been processed and the detection results have been successfully validated using AIS data.

Due to some technological limitations of TerraSAR-X, a nonoptimal PRI sequence and chirp bandwidth had to be used for this experiment. While the use of a nonoptimal PRI sequence has resulted in range ambiguities from ships still being above the detection threshold, their specific signature due to the PRI variation has still allowed for a clear discrimination between the ships and their ambiguities. Iterative subtraction of the impulse responses of each detected target (as in the CLEAN algorithm) or the use of an extended matching filter (that includes the ambiguities) could be useful and investigated in the future for the rejection of range ambiguities. Advanced detection techniques may aid in automating the rejection of artifact-caused false alarms.

The experiment is significant because it has the potential to serve as a test bed for the validation of the ambiguous mode for ship monitoring. The exploitation of ambiguous modes can go beyond the monitoring of ships in open sea and be extended to other applications, such as deformation monitoring using permanent scatterers interferometry.

Further experimental acquisitions are planned that also exploit waveform diversity in combination with the ambiguous modes, such as an alternating of up- and down-chirp [48], [49]. This approach facilitates the complete smearing of first-order range ambiguities, even in cases, such as TerraSAR-X, where a more elaborated PRI sequence with finer PRI variation is not feasible.

ACKNOWLEDGMENT

The authors would like to thank their colleagues of the Maritime Security Lab of DLR's German Remote Sensing Data Center in Neustrelitz for many fruitful discussions and Vesselfinder Limited and MaritimeTraffic for providing the AIS datasets.

REFERENCES

[1] K. Eldhuset, "An automatic ship and ship wake detection system for spaceborne SAR images in coastal regions," *IEEE Trans. Geosci. Remote Sens.*, vol. 34, no. 4, pp. 1010–1019, Jul. 1996.

[2] P. W. Vachon, J. W. M. Campbell, C. A. Bjerkelund, F. W. Dobson, and M. T. Rey, "Ship detection by the RADARSAT SAR: Validation of detection model predictions," *Can. J. Remote Sens.*, vol. 23, no. 1, pp. 48–59, Mar. 1997.

[3] S. Brusch, S. Lehner, T. Fritz, M. Soccorsi, A. Soloviev, and B. van Schie, "Ship surveillance with TerraSAR-X," *IEEE Trans. Geosci. Remote Sens.*, vol. 49, no. 3, pp. 1092–1103, Mar. 2011.

[4] D. Crisp, "The state-of-the-art in ship detection in synthetic aperture radar imagery," Defence Sci. Technol. Org., Port Wakefield, SA, Australia, Res. Rep. DSTO-RR-0272, 2004.

[5] P. Lombardo and M. Sciotti, "Segmentation-based technique for ship detection in SAR images," *IEE Proc.-Radar, Sonar Navigat.*, vol. 148, no. 3, p. 147, 2001.

[6] D. Pastina, F. Fico, and P. Lombardo, "Detection of ship targets in COSMO-SkyMed SAR images," in *Proc. IEEE Radar Conf. (RADAR)*, May 2011, pp. 928–933.

[7] H. Greidanus, M. Alvarez, C. Santamaria, F.-X. Thoorens, N. Kourti, and P. Argentieri, "The SUMO ship detector algorithm for satellite radar images," *Remote Sens.*, vol. 9, no. 3, p. 246, Mar. 2017.

[8] Q. Jiang et al., "Ship detection in RADARSAT SAR imagery," in *Proc. IEEE Int. Conf. Syst., Man, Cybern.*, May 1998, pp. 4562–4566.

[9] P. Iervolino and R. Guida, "A novel ship detector based on the generalized-likelihood ratio test for SAR imagery," *IEEE J. Sel. Topics Appl. Earth Observ. Remote Sens.*, vol. 10, no. 8, pp. 3616–3630, Aug. 2017.

[10] P. W. Vachon, J. Wolfe, and H. Greidanus, "Analysis of Sentinel-1 marine applications potential," in *Proc. IEEE Int. Geosci. Remote Sens. Symp.*, Jul. 2012, pp. 1734–1737.

[11] H. Greidanus et al., "Benchmarking operational SAR ship detection," in *Proc. IEEE Int. IEEE Int. Geosci. Remote Sens. Symp.*, Feb. 2004, pp. 4215–4218.

[12] C. H. Gierull and I. Sikaneta, "A compound-plus-noise model for improved vessel detection in non-Gaussian SAR imagery," *IEEE Trans. Geosci. Remote Sens.*, vol. 56, no. 3, pp. 1444–1453, Mar. 2018.

[13] J. Krecke, M. Villano, N. Ustalli, A. C. M. Austin, J. E. Cater, and G. Krieger, "Detecting ships in the New Zealand exclusive economic zone: Requirements for a dedicated SmallSat SAR mission," *IEEE J. Sel. Topics Appl. Earth Observ. Remote Sens.*, vol. 14, pp. 3162–3169, 2021.

[14] N. Ustalli, G. Krieger, and M. Villano, "A low-power, ambiguous synthetic aperture radar concept for continuous ship monitoring," *IEEE J. Sel. Topics Appl. Earth Observ. Remote Sens.*, vol. 15, pp. 1244–1255, 2022.

[15] A. Freeman et al., "The 'Myth' of the minimum SAR antenna area constraint," *IEEE Trans. Geosci. Remote Sens.*, vol. 38, no. 1, pp. 320–324, Jan. 2000.

[16] K. Tomiyasu, "Conceptual performance of a satellite borne, wide swath synthetic aperture radar," *IEEE Trans. Geosci. Remote Sens.*, vol. GE-19, no. 2, pp. 108–116, Apr. 1981.

[17] F. De Zan and A. M. Guarnieri, "TOPSAR: Terrain observation by progressive scans," *IEEE Trans. Geosci. Remote Sens.*, vol. 44, no. 9, pp. 2352–2360, Sep. 2006.

[18] J. Márquez-Martínez, M. Cohen, S. Doody, P. Lau-Semedo, and A. Larkins, "Next generation low cost SAR payloads: NovaSAR-S and beyond," in *Proc. IEEE Int. Geosci. Remote Sens. Symp. (IGARSS)*, Fort Worth, TX, USA, Jul. 2017, pp. 3848–3851.

[19] M. Cohen, A. Larkins, P. L. Semedo, and G. Burbidge, "NovaSAR-S low cost spaceborne SAR payload design, development and deployment of a new benchmark in spaceborne radar," in *Proc. IEEE Radar Conf. (RadarConf)*, Seattle, WA, USA, May 2017, pp. 903–907.

[20] N. Goodman, D. Rajakrishna, and J. Stiles, "Wide swath, high resolution SAR using multiple receive apertures," in *Proc. IEEE Int. Geosci. Remote Sens. Symp.*, Oct. 1999, pp. 1767–1769.

[21] N. Gebert, G. Krieger, and A. Moreira, "Digital beamforming for HRWS-SAR imaging: System design, performance and optimization strategies," in *Proc. IEEE Int. Symp. Geosci. Remote Sens.*, Jan. 2006, pp. 1836–1839.

[22] G. Krieger, N. Gebert, and A. Moreira, "Unambiguous SAR signal reconstruction from nonuniform displaced phase center sampling," *IEEE Geosci. Remote Sens. Lett.*, vol. 1, no. 4, pp. 260–264, Oct. 2004.

[23] G. Di Martino and A. Iodice, "Coprime synthetic aperture radar (CopSAR): A new acquisition mode for maritime surveillance," *IEEE Trans. Geosci. Remote Sens.*, vol. 53, no. 6, pp. 3110–3123, Jun. 2015.

[24] G. Di Martino and A. Iodice, "Orthogonal coprime synthetic aperture radar," *IEEE Trans. Geosci. Remote Sens.*, vol. 55, no. 1, pp. 432–440, Jan. 2017.

[25] N. Ustalli and M. Villano, "High-resolution wide-swath ambiguous synthetic aperture radar modes for ship monitoring," *Remote Sens.*, vol. 14, no. 13, p. 3102, Jun. 2022, doi: 10.3390/rs14133102.

[26] M. Villano, G. Krieger, and A. Moreira, "Advanced spaceborne SAR systems with planar antenna," in *Proc. IEEE Radar Conf. (RadarConf)*, Seattle, WA, USA, May 2017, pp. 0152–0156.

[27] M. Villano, G. Krieger, and A. Moreira, "Staggered SAR: High-resolution wide-swath imaging by continuous PRI variation," *IEEE Trans. Geosci. Remote Sens.*, vol. 52, no. 7, pp. 4462–4479, Jul. 2014.

[28] M. Villano, G. Krieger, and A. Moreira, "A novel processing strategy for staggered SAR," *IEEE Geosci. Remote Sens. Lett.*, vol. 11, no. 11, pp. 1891–1895, Nov. 2014.

[29] M. Villano, G. Krieger, M. Jäger, and A. Moreira, "Staggered SAR: Performance analysis and experiments with real data," *IEEE Trans. Geosci. Remote Sens.*, vol. 55, no. 11, pp. 6617–6638, Nov. 2017.

[30] M. Villano, "Staggered synthetic sperture radar," Ph.D. Thesis, Karlsruhe Institute of Technology, Wessling, Germany, 2016.

[31] M. Pinheiro et al., "Processing and performance analysis of NASA-ISRO SAR (NISAR) staggered data," in *Proc. IEEE Int. Geosci. Remote Sens. Symp.*, Yokohama, Japan, Jul. 2019, pp. 8374–8377.

[32] M. Pinheiro, P. Prats-Iraola, M. Rodriguez-Cassola, and M. Villano, "Combining spectral estimation and BLU interpolation for the reconstruction of low-oversampled staggered SAR data," in *Proc. 12th Eur. Conf. Synth. Aperture Radar*, Aachen, Germany, Jun. 2018, pp. 1–6.

[33] M. Pinheiro, P. Prats-Iraola, M. Rodriguez-Cassola, and M. Villano, "Analysis of low-oversampled staggered SAR data," *IEEE J. Sel. Topics Appl. Earth Observ. Remote Sens.*, vol. 13, pp. 241–255, 2020.

[34] M. Villano, G. Krieger, and A. Moreira, "Ambiguities and image quality in staggered SAR," in *Proc. IEEE 5th Asia–Pacific Conf. Synth. Aperture Radar (APSAR)*, Singapore, Sep. 2015, pp. 204–209.

[35] M. Villano et al., "Gapless imaging with the NASA-ISRO SAR (NISAR) mission: Challenges and opportunities of staggered SAR," in *Proc. 12th Eur. Conf. Synth. Aperture Radar*, Aachen, Germany, Jun. 2018, pp. 1–6.

[36] M. Younis, F. Q. de Almeida, M. Villano, S. Huber, G. Krieger, and A. Moreira, "Digital beamforming for spaceborne reflector-based synthetic aperture radar, Part 1: Basic imaging modes," *IEEE Geosci. Remote Sens. Mag.*, vol. 9, no. 3, pp. 8–25, Sep. 2021.

[37] M. Younis, F. Q. D. Almeida, M. Villano, S. Huber, G. Krieger, and A. Moreira, "Digital beamforming for spaceborne reflector-based synthetic aperture radar, Part 2: Ultrawide-swath imaging mode," *IEEE Geosci. Remote Sens. Mag.*, vol. 10, no. 4, pp. 10–31, Dec. 2022.

[38] M. Quintana et al., "Perteo: Persistent real-time Earth observation small satellite constellation for natural disaster management," in *Proc. IEEE Int. Geosci. Remote Sens. Symp.*, Jul. 2023, pp. 1–6.

[39] R. Werninghaus and S. Buckreuss, "The TerraSAR-X mission and system design," *IEEE Trans. Geosci. Remote Sens.*, vol. 48, no. 2, pp. 606–614, Feb. 2010.

[40] M. Villano and M. N. Peixoto, "Characterization of nadir echoes in multiple-elevation-beam SAR with constant and variable pulse repetition interval," *IEEE Trans. Geosci. Remote Sens.*, vol. 60, 2022, Art. no. 5215609.

[41] I. G. Cumming and F. H. Wong, *Digital Processing of Synthetic Aperture Radar Data: Algorithms and Implementation*. Norwood, MA, USA: Artech House, 2005.

[42] B. B. Smestad, B. E. Asbjørnslett, and Ø. J. Rødseth, "Expanding the possibilities of AIS data with heuristics," *TransNav, Int. J. Mar. Navigat. Saf. Sea Transp.*, vol. 11, no. 2, pp. 93–100, 2017.

[43] E. Schwarz, D. Krause, S. Voinov, H. Daedelow, and S. Lehner, "Near real time applications for maritime situational awareness," in *Proc. 4th Int. Conf. Remote Sens. Geoinf. Environ.*, Paphos, Cyprus, Apr. 2016, pp. 4–8.

[44] S. Voinov, E. Schwarz, D. Krause, and M. Berg, "Identification of SAR detected targets on sea in near real time applications for maritime surveillance," in *Proc. Free Open Source Softw. Geospatial Conf.*, 2016, p. 16, doi: 10.7275/R5125QTW.

[45] (2022). *VesselFinder*. Accessed: Nov. 22, 2022. [Online]. Available: https://www.vesselfinder.com/

[46] (2022). *MarinTraffic*. Accessed: Nov. 22, 2022. [Online]. Available: https://www.marinetraffic.com/

[47] P. W. Vachon, R. A. English, and J. Wolfe, *Ship Signatures in RADARSAT-1 ScanSAR Narrow B Imagery Analysis With AIS Live Data*. Ottawa, ON, Canada: Technical Memorandum DRDC, 2007, pp. 1–44.

[48] S.-Y. Jeon, T. Kraus, U. Steinbrecher, M. Villano, and G. Krieger, "A TerraSAR-X experiment for validation of nadir echo suppression through waveform encoding and dual-focus post-processing," in *Proc. 13th Eur. Conf. Synth. Aperture Radar*, Mar. 2021, pp. 1–5.

[49] N. Ustalli and M. Villano, "Impact of ambiguity statistics on information retrieval for conventional and novel SAR modes," in *Proc. IEEE Radar Conf.*, Florence, Italy, Sep. 2020, pp. 1–6.

Nertjana Ustalli (Member, IEEE) received the M.Sc. degree (Hons.) in communication engineering and the Ph.D. degree (Hons.) in radar and remote sensing from the Sapienza University of Rome, Rome, Italy, in 2014 and 2018, respectively.

From July 2018 to June 2019, she was a Post-Doctoral Researcher with the Department of Information Engineering Electronics and Telecommunications (DIET), Sapienza University of Rome, where she worked on the development of detection and motion parameters estimation techniques for moving targets in forward scatter radar configuration. Since October 2019, she has been with the Microwaves and Radar Institute, German Aerospace Center (DLR), Wessling, Germany. Her research interests include the development of cost-effective synthetic aperture radar (SAR) for dedicated applications, the investigation of phase synchronization approaches for small-satellite SAR constellations, and the analysis of ambiguities in conventional and waveform-encoded SAR modes.

Dr. Ustalli was a recipient of the Best Student Paper Award at the 2017 International Conference on Radar Systems, the Best Paper Award at the 2018 International Radar Symposium, the Best Paper Award at the 2018 GTTI Workshop on Radar and Remote Sensing, the Best 2018 Ph.D. Theses in the field of Communication Technologies defended at an Italian university, and the Young Scientist Award at the 2022 Kleinheubacher Tagung organized by the International Union of Radio Science.

Maxwell Nogueira Peixoto (Graduate Student Member, IEEE) was born in Feira de Santana, Bahia, Brazil, in 1996. He received the B.S. degree in electronic engineering and the M.S. degree in telecommunications from the Aeronautics Institute of Technology (ITA), São José dos Campos, São Paulo, Brazil, in 2020 and 2021, respectively. He is currently pursuing the Ph.D. degree in electronic engineering with Ulm University, Ulm, Germany, and the Microwave and Radar Institute, German Aerospace Center (DLR), Wessling, Germany.

In 2019, he was an Intern at the Microwaves and Radar Institute, DLR, where he worked at the NewSpace SAR Research Group on the topic of nadir echo characterization and suppression in staggered SAR. In 2021, he returned to the NewSpace SAR Research Group, Microwaves and Radar Institute, DLR, where he currently doing research on the topic of distributed SAR interferometry using clusters of SmallSats. His research interests include radar signal processing, staggered SAR, and multibaseline SAR interferometry.

Mr. Nogueira Peixoto was a recipient of the Young Scientist Award at the Kleinheubacher Tagung 2021, Miltenberg, Germany, and the Second Place 2023 Student Prize Paper Award at the IEEE International Geoscience and Remote Sensing Symposium (IGARSS), Pasadena, CA, USA, in 2023.

Thomas Kraus received the M.Sc. degree in electrical engineering from the University of Ulm, Ulm, Germany, in 2009.

In 2010, he joined the Microwaves and Radar Institute, German Aerospace Center (DLR), Wessling, Germany, where he is currently working in the field of spaceborne SAR. He is involved in the instrument commanding, processing, and analysis of scientific and experimental acquisitions in the framework of the projects TerraSAR-X and TanDEM-X. He was responsible for the performance analysis during the operational implementation of the Staring Spotlight and the wide ScanSAR modes of TerraSAR-X as well as the dual receive antenna mode in the bistatic science phase of TanDEM-X. For the geostationary mission proposal Hydroterra, he also contributed to the SAR performance analysis. His research interests include radar system performance, the development of innovative SAR modes, and the analysis of distributed satellite SAR systems.

Ulrich Steinbrecher received the Dipl.-Ing. degree in electrical engineering/communication from the University of Siegen, Siegen, Germany, in 1990.

In 1990, he started his career with the German Aerospace Center, Wessling, Germany, with the development of an SAR raw data simulator. Then, he was in software development with the X-SAR Processor and with the joint U.S.–Italian–German SIR-C/XSAR Missions in 1994. When the data were in house, he concentrated on aspects of the operational SAR processing of high data volumes. In 1995, he pioneered a completely automatic SAR processing system based on a robot maintained mass memory archive. Before he became responsible for the development of the raw data analysis and screening system for the shuttle radar topography mission, he developed the software for a phase-preserving ScanSAR processor for Radarsat-1. In the time between the SRTM mission and the start of the TerraSAR-X project, he left the SAR domain for two years and contributed to the SCIAMACHY LIMB processing system. Since 2002, he has been concerned with the TerraSAR-X radar system, and since the launch of the satellite, in 2007, he was responsible for TerraSAR-X instrument operations.

Gerhard Krieger (Fellow, IEEE) received the Dipl.-Ing. (M.S.) and Dr.-Ing. (Ph.D.) (Hons.) degrees in electrical and communication engineering from the Technical University of Munich, Munich, Germany, in 1992 and 1999, respectively.

From 1992 to 1999, he was with Ludwig Maximilians University, Munich, where he conducted multidisciplinary research on neuronal modeling and nonlinear information processing in biological and technical vision systems. Since 1999, he has been with the Microwaves and Radar Institute, German Aerospace Center (DLR), Wessling, Germany, where he started as a Research Associate developing signal processing algorithms for a novel forward-looking radar system employing digital beamforming on receive. From 2001 to 2007, he led the New Synthetic Aperture Radar (SAR) Missions Group, which pioneered the development of advanced bistatic and multistatic radar systems, such as TanDEM-X, as well as innovative multichannel SAR techniques and algorithms for high-resolution wide-swath SAR imaging. Since 2008, he has been the Head of the Radar Concepts Department, which currently hosts about 50 scientists focusing on new SAR techniques, missions, and applications. He has been serving as a Mission Engineer for TanDEM-X and he made also major contributions to the development of the Tandem-L mission concept, where he led the Phase-0 and Phase-A studies. Since 2019, he has been holding also professorship with Friedrich-Alexander-University Erlangen, Erlangen, Germany. He is the author or a coauthor of more than 100 peer-reviewed journal articles, nine invited book chapters, over 500 conference papers, and holds more than 20 patents.

Prof. Krieger received several national and international awards, including the two Best Paper Awards from the European Conference on SAR, the two Transactions Prize Paper Awards from the IEEE Geoscience and Remote Sensing Society, and the W.R.G. Baker Prize Paper Award from the IEEE Board of Directors. In 2014, he served as the Technical Program Chair for the European Conference on SAR and a Guest Editor for the IEEE JOURNAL OF SELECTED TOPICS IN APPLIED EARTH OBSERVATIONS AND REMOTE SENSING. He has been an Associate Editor for IEEE TRANSACTIONS ON GEOSCIENCE AND REMOTE SENSING since 2012.

Michelangelo Villano (Senior Member, IEEE) received the B.Sc. and M.Sc. degrees (Hons.) in telecommunication engineering from the Sapienza University of Rome, Rome, Italy, in 2006 and 2008, respectively, and the Ph.D. degree (Hons.) in electrical engineering and information technology from the Karlsruhe Institute of Technology, Karlsruhe, Germany, in 2016.

From 2008 to 2009, he was a Young Graduate Trainee with the European Space Research and Technology Center, European Space Agency, Noordwijk, The Netherlands, where he developed processing algorithms for ice sounding radar. Since 2009, he has been with the Microwaves and Radar Institute, German Aerospace Center (DLR), Wessling, Germany, where he developed, among others, the staggered synthetic aperture radar (SAR) acquisition mode that allows imaging a wide swath with high resolution through continuous variation of the pulse repetition interval. Since 2019, he has been the Head of the NewSpace SAR Research Group, where he leads the development of cost-effective and multistatic SAR concepts for frequent and enhanced Earth monitoring. In 2017, he was a Visiting Research Scientist with the Communications, Tracking, and Radar Division, NASA Jet Propulsion Laboratory, Pasadena, CA, USA, where he adapted the staggered SAR mode to the NASA-ISRO SAR (NISAR) mission, for which staggered SAR is the baseline acquisition mode. Since 2019, he has also been a Lecturer with Ulm University, Ulm, Germany. He has authored or coauthored over 35 peer-reviewed journal papers, a book chapter, and over 90 articles in international conference proceedings. He holds 11 patents in the field of SAR.

Dr. Villano was a recipient of the First Place Student Paper Award at the European Conference on Synthetic Aperture Radar (EUSAR), Berlin, Germany, in 2014; the IEEE Geoscience and Remote Sensing Society Letters Prize Paper Award in 2015 and 2017; the Student Paper Award at the Asia–Pacific Conference on Synthetic Aperture Radar, Marina Bay Sands, Singapore, in 2015; the DLR Science Award in 2016 and 2023; the Award as Young Scientist of the Foundation Werner von Siemens Ring in 2017; the ITG Dissertation Award in 2017; and the Best Paper Award at the German Microwave Conference 2019. In 2022, he was awarded a Starting Grant by the European Research Council (ERC). He is the Co-Chair of the Working Group on "Active Microwave: Radar and SAR" of the IEEE Geoscience and Remote Sensing Society's Technical Committee on Instrumentation and Future Technologies. He serves as an Associate Editor for IEEE TRANSACTIONS OF GEOSCIENCE AND REMOTE SENSING. He serves as the Technical Program Chair for the EUSAR 2024.